Ultrastructure analysis of cardiomyocytes and their nuclei

Tabish A. Syed[1 [0000−0002−6987−4975]], Yanan Wang[1 [0000−0002−4427−8667]], Drisya Dileep[2,3 [0000−0002−7871−5343]], Minhajuddin Sirajuddin[2 [0000−0001−5742−2130]], and Kaleem Siddiqi[1 [0000−0002−7347−9716]]

[1] School of Computer Science, McGill University, Montréal, Canada
[2] Institute for Stem Cell Science and Regenerative Medicine, Bengaluru, India
[3] The University of Trans-Disciplinary Health Sciences and Technology (TDU), Bengaluru, India

Abstract. Cardiomyocytes are elongated and densely packed in the mammalian heart and connected end on end to achieve a functional syncytium. Qualitative accounts describe their nuclei as being elongated in their long axis direction, which might help to better distribute mechanical load and reduce mechanical stress during contraction. Alterations of nuclear orientation and shape have also been known to be associated with certain cardiomyopathies. Yet, to date, the alignment of cardiomyocytes and their nuclei at the cellular (micron) scale has not been assessed in a quantitative fashion. To examine this we developed 3D computer vision methods to segment myocytes and their nuclei in cleared and membrane stained thick 3D tissue sections from a wild type mouse heart, imaged using confocal microscopy. We extended a geometric flow based superpixel algorithm to 3D and then adaptively merged the resulting supervoxels to recover individual myocytes. In parallel we also applied recent popular deep learning based cell segmentation methods to the same data. Our experiments revealed a close alignment of myocyte orientation with nucleus orientation, with a median difference of approximately 10 degrees, and also showed that most cardiomyocytes contain only one or two nuclei. These findings pave the way for future investigations of the effect of specific cardiac diseases on nuclear shape, elongation and number.

Keywords: cardiomyocytes · nuclei · tissue clearing · staining · confocal microscopy · cell segmentation · orientation analysis

1 Introduction

The morphology of nuclei within cardiomyocytes is known to play an important role in their development. Nuclei can be reshaped when these cells are under a tensile load and gene expression can be altered by changes in nuclear morphology, potentially signalling aberrant patient conditions [18]. The contraction of cardiomyocytes also distributes mechanical forces within them, affecting their internal structure [4]. Nuclear rearrangement can also evolve into disorders that are manifest in elderly individuals as cardiovascular disease or hypertension [15].

Cardiomyopathies can also affect nuclei within cardiomyocytes. For example, hypertrophic cardiomyopathy is correlated with a reduction in nuclear deformation and reduction in the frequency of contractions, while dilated cardiomyopathy induced by laminopathies can alter the circularity, morphology, and orientation of nuclei [5, 3]. Nuclear morphology is thus highly correlated with healthy function and the possibility of assessing cardiomyocyte and nucleus shape, structure and orientation from tissue samples could provide both diagnostic and therapeutic benefits.

Recent work has examined how tensile loads, coupled with the action of certain proteins, can result in an in situ deformation of a cell [1]. Rows of cell nuclei within the field of view are seen moving in opposite directions, changing the orientation of their long axis, and falling in and out of the focal plane. Using phase contrast/polarization microscopy the role of cytoskeletal proteins and integrins in determining cell shape and nuclear re-orientation induced strain is examined in [13]. When integrin proteins are distorted with a strain, the actin cytoskeletal filaments re-orient and the nucleus aligns with and elongates in the long-axis direction of the applied tension field. Myocyte orientation has also been studied in tissue engineering. For example, when grown on flat substrates cardiomyocytes exhibit no particular orientation preference, and the nuclei are isotropic or circular in shape [8]. However, when a complex scaffold is used as a substrate the cells self organize into oriented structures. The nuclei then become elongated along the cell long axis direction, and the cells exhibit persistent mechanical and electrical activity. In fact, the importance of orientation dependent alterations to cardiomyocyte shape, e.g., in the presence of cardiomyopathy, is recognized [5]. Incidences of polyploidy and multi nucleation have been studied across species [7, 14], but a thorough quantitative analysis of the number of nuclei within cardiomyocytes has not yet been performed.

To potentially address this, workflows for segmenting individual cardiomyocytes, by isolating the interior of mitochondria and myofibrils, have been proposed [10]. Such methods rely on adaptive thresholding and on the manual delineation of myocyte boundaries. Related approaches in [2] for cell shape analysis also rely on thresholding and thus generalizations to handle large sections of heart tissue are not obvious. Thus, few methods presently exist for automated ultrastructure shape analysis of heart tissue at the micron scale of cardiomyocytes. Motivated by this, we developed methods for ultrastructure analysis of cardiomyocytes at the micron scale. We first prepared cleared heart tissue samples using a CLARITY based protocol [6] and imaged thick stacks using confocal microscopy. We then considered two different classes of algorithms. The first (bottom up) approach began with an oversegmentation using an extension of the popular geometric flow based Turbopixel [11] algorithm to 3D. This was followed by a greedy merge procedure designed to coalesce Turbovoxels that were connected at interfaces free of the WGA membrane stain and were thus likely to lie within the same cardiomyocyte. The second (top down) approach used current trained neural networks for single cell segmentation [17, 9]. Both approaches provided quantitative verification of nuclear alignment with cardiomyocytes in

excised wild type mouse heart tissue, and further revealed that cardiomyocytes have only a few nuclei. The methods and findings in this paper pave the way for future quantitative studies of the effects of cardiomyopathies on cardiomyocyte and nucleus shape and alignment.

2 Methods

2.1 Tissue Sample Preparation and Imaging

A mouse heart was excised after perfusion with ice-cold 1X PBS, 4% PFA, and then incubated in a hydrogel solution for several days. The hydrogel was polymerized at 37 degree Celsius, fixing the heart samples in a hydrogel matrix. The heart tissue was then allowed to passively undergo clearing passively by incubating in a clearing buffer, following the CLARITY protocol [6]. The cleared heart was sectioned by a compressotome to generate sections of width 500 μm perpendicular to its long axis. Heart sections selected from the mid-ventricular region were processed for staining with fluorescently labeled WGA (wheat germ agglutinin) and DAPI, which marked cell membranes and nuclei, respectively. We used an Olympus FV3000 confocal microscope with a 60X/1.4NA oil objective for imaging. The imaging regions were concentrated near the mid-LV wall where cardiomyocytes were largely in the plane of imaging in each short axis section, as demonstrated in Fig. 1 (top left). We selected 15 stacks of size $320 \times 320 \times 150$ voxels, with each voxel being $.66 \times .66 \times .8\ \mu m^3$ in size, for analysis.

2.2 Geometric Flow Based Segmentation

Turbovoxels Our first method is a 3D extension of the 2D geometric flow based Turbopixel algorithm [11], which we dub "Turbovoxels". The algorithm is designed to provide a dense segmentation of the image space into compact regions while respecting boundaries, where a typical structure of interest would be comprised of a connected group of such regions. Thus it provides a useful first step in the recovery of densely packed cells whose membranes have been stained. The algorithm is implemented using a narrow-band level sets method [16], which represents the supervoxel boundaries as the zero level surfaces of an embedding function Φ. The flow based design of Turbovoxels allows for the choice of initial seed locations and their number. We first divide the 3D image volume into a uniform cuboidal grid of size $G_x \times G_y \times G_z$, based on the number of seeds to place within each grid block. Then, within each grid block, we place a seed at the location of minimum intensity of the WGA stain, to ensure that the initial seeds are distant from the brightly stained cell membranes. In our dataset containing image volumes of size $320 \times 320 \times 150$ voxels, we used a seed count of 5000. This corresponds to roughly one supervoxel per cube of length $10\mu m$ in each of its dimensions, which is around half the width of a typical myocyte in a mouse heart. The initial level set embedding Φ is constructed from the Euclidean signed distance function of spheres of radius 3, centered at the seed locations,

as illustrated in Figure 1 (bottom, middle) for a 2D slice of a sample region. Using the standard level set framework the evolution of the embedding level set function Φ is given by

$$\frac{\partial \Phi}{\partial t} = -S||\nabla \Phi|| \tag{1}$$

where S, the speed function, determines the speed of evolution in the direction of the normal to a point on the surface of an evolving supervoxel. Following [11] we factor the speed function into a product $S = S_I S_B$ of an intensity term S_I and a boundary term S_B. The boundary term is a function of distance to the nearest supervoxel. S_B is set to zero for voxels that are equidistant from the boundaries of more than one supervoxel. This multiplicative speed function ensures that supervoxel boundaries do not cross and the resulting Turbovoxels are simply-connected. The boundary term can be evaluated efficiently by first computing the medial surface of the background and setting the term to 0 at locations coincident with the medial surface and to 1 elsewhere. In practice, for efficiency, we approximate a thick medial surface by removing background voxels iteratively while using a digital homotopy preserving method, as described in [12]. The intensity term S_I is based on a linear combination of a constant, curvature and doublet term [11]:

$$S_I = \psi(\mathbf{x}) + \alpha\kappa(\mathbf{x})\psi(\mathbf{x}) + \beta N(\mathbf{x}).\nabla\psi(\mathbf{x}).$$

In our implementation we set the weight α to 0.2 and the doublet weight β to 0.3. The curvature term ensures that the boundaries of supervoxels are smooth, while the doublet term attracts the evolving boundaries to the edges as defined by the edge strength function $\psi = e^{\frac{-|\nabla I|}{G_\sigma * |\nabla I| + \gamma}}$ [11], where I is the image intensity, G_σ is a Gaussian kernel with standard deviation σ, and γ is a scaling factor, which was empirically set to 10. The right panels in Figure 1 depict the final boundaries of the Turbovoxels (overlayed in cyan) while the middle panels show the zero levelset of the evolving fronts at three time points of the evolution.

Merging We then merged Turbovoxels into larger segments (Turboblobs) using a criterion that takes into account the membrane stain at the interface of two Turbovoxels. For all Turbovoxel pairs that share a common boundary we compute an affinity term that is inversely proportional to the average stain intensity at their interface. We then employ a 2-stage greedy approach. In the first stage, a Turbovoxel is merged with at most one of its neighbors, the one that it is closest to in terms of the affinity score, provided that their common surface area is above a threshold. This process is carried out in 3D over the entire volume, giving rise to larger groups of Turbovoxels, and is applied for two iterations. At the end of the first stage, the segments consist of one, two or four original Turbovoxels. In the second stage, we first construct a minimum heap using all pairs of neighbouring segments with the affinity term as the sorting key. We then carry out greedy pairwise merges, in an iterative manner, resulting in

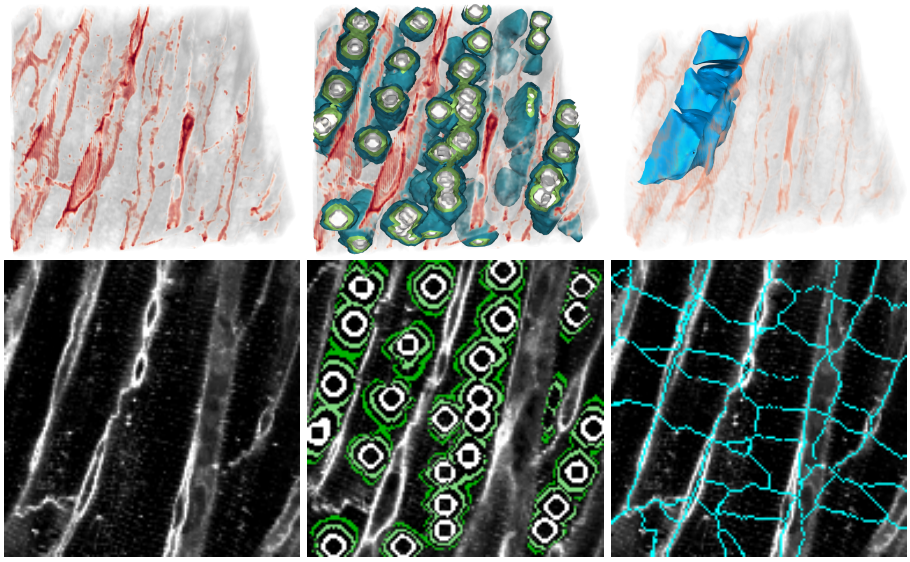

Fig. 1. Top: A 3D stack of cleared mouse tissue, with the WGA stain highlighting membranes shown in red (left). Seeds evolve outwards, with iterations shown in green to blue (middle). The medial surface between them prevents merging, and an edge-strength based stopping term slows the fronts down in the vicinity of cell membranes. A few of the final dense Turbovoxels are overlayed on the WGA stain in cyan (right). Bottom: A 2D slice of the respective panels on the top. Typical results showing merged Turbovoxels are shown in Fig. 3 (bottom right).

larger Turboblobs. The pair with the lowest average intensity at their interface (highest affinity) is merged first. The merged Turboblob is then inserted into the heap, with the affinities of all its neighbouring blobs recomputed. The process is repeated in an iterative manner, with merges allowed only if a threshold on affinity is reached, until it converges, i.e., no additional merges can be applied.

Run Time Our implementation of Turbovoxels has not been optimized or parallelized, and thus is not yet suited for real time processing. For a single volume it takes on the order of 4 hrs for their computation on an Intel(R) Core(TM) i9-7900X processor, with an additional 5 minutes for the merging step.

2.3 Neural Network Based Segmentation

Neural network based approaches for cell segmentation use pre-trained models to produce initial segmentations. Given application specific examples with labeled ground truth results, the network weights can be fine-tuned to produce final results. In the realm of myocyte segmentation from membrane stained data,

few (if any) labeled data sets presently exist. We chose to experiment with two networks that represent the present state of the art: Cellpose [17] and Mesmer [9]. Cellpose uses a modified U-Net backbone with residual building blocks, predicting two pixel-wise probability maps. The first classifies a pixel as background or interior, while the second, a spatial gradient mask, learns the gradient of a distance function from the center of a cell. Cellpose also provides a 3D extension of its 2D models. The 3D extension generates 3 separate cell probability maps for three 90 degree rotations of the volume, and the corresponding 3 predicted 2D gradient maps.

Mesmer uses a ResNet50 backbone-based feature pyramid network and a watershed post-processing step and is pre-trained on TissueNet, which has more than 1 million (2D) labelled cells obtained through crowd-sourcing. Being a 2D method, we had to apply a stitching approach based on intersection over union between successive slices, to obtain labels in 3D.

For segmenting nuclei we found that Cellpose performed well on the DAPI channel, using its pre-trained "nucleus" model. The model was set to operate in 3D, enabling segmentation across all XY, XZ, and YZ slices. However, when applied to the original WGA stained membrane data with the "cytoplasm" option, the model gave poor results for myocyte segmentation, likely due to its bias towards interior texture in the data it is pre-trained on. Such texture is almost completely absent in the interior of elongated myocytes in a membrane channel. To improve its performance, motivated by the construction in [11], we chose to first apply the same edge-strength based speed function used for Turbovoxels, described in Section 2.2, to the WGA channel. This function is designed to highlight boundaries while placing texture within (Fig. 3 shows a typical case), and in practice gave far improved segmentation results.

Run Time Running both the Cellpose and Mesmer models on an Intel(R) Xeon(R) CPU @ 2.30GHz with a GPU Tesla T4 takes approximately 5 minutes per volume.

2.4 Orientation Analysis and Fractional Anisotropy

For each segmented nucleus and myocyte we estimated its orientation using an eigenvalue/eigenvector decomposition of the associated 3D covariance matrix of each binary object. The covariance matrix defined as $cov(x_i, x_j) = \mathbf{E}[(x_i - \mathbf{E}[x_i])(x_j - \mathbf{E}[x_j])^T]$, where $\mathbf{E}()$ is the expected value of object voxel coordinates x_i. The covariance matrix quantifies the spread of object coordinates (x_i) about the centroid ($\mathbf{E}[x_i]$). Specifically, given a binary segmented object, its orientation was taken to be that corresponding to the eigenvector of the covariance matrix associated with the largest eigenvalue. Further, with $\lambda_1, \lambda_2, \lambda_3$ being the eigenvalues, a measure of its elongation from $[0, 1]$ was obtained by computing the fractional anisotropy (FA) measure

$$FA = \sqrt{\frac{1}{2}} \frac{\sqrt{(\lambda_1 - \lambda_2)^2 + (\lambda_2 - \lambda_3)^2 + (\lambda_3 - \lambda_1)^2}}{\sqrt{\lambda_1^2 + \lambda_2^2 + \lambda_3^2}}.$$

3 Results

3.1 Elongation of Cardiomyocytes and their Nuclei

For nuclei the mode of the FA measure over all datasets was found to be 0.84 with the median being 0.74, with a 95% confidence interval of $(0.7337, 0.7419)$. For myocytes, the mode of the FA measure over all datasets, shown in Fig. 2, was found to be 0.95 or higher. These measurements indicate that both nuclei and myocytes are highly oriented structures.

Method	FA mode	FA median	median CI
Turbovoxels	0.9483	0.9243	(0.9201, 0.9279)
Cellpose	0.9725	0.9501	(0.9489, 0.9514)
Mesmer	0.9475	0.9085	(0.9061, 0.9105)
GT	0.9628	0.9527	(0.9453, 0.9599)

Fig. 2. Fractional Anisotropy(FA) analysis of segmented myocytes across entire dataset, using the Turbovoxels, Cellpose and Mesmer methods and also a single 3D image with hand segmented labels (GT). The Table lists the mode in column 2, the median in column 3 and the 95% confidence intervals of the respective medians in column 4.

3.2 Orientation Comparison

Our segmentations enabled us to determine the number of nuclei contained in each cardiomyocyte and to compare their orientations. Fig. 4 (bottom) shows polar histograms of the magnitude of the angular difference in degrees using the 3 different methods. Turbovoxels gave a median orientation difference of 11.9° with a 95% confidence interval (CI) of $(11.5, 12.4)$. The median orientation differences using Cellpose and Mesmer were 11.6° CI of $(11.2, 12.1)$) and 11.6° (CI of $(11.1, 12.1)$), respectively. To validate our auto-segmentations we hand segmented all the myocytes in one 3D volume. For each auto-segmented myocyte in an image volume, we picked the ground truth segment with the maximum volume overlap and computed the Dice score between them. The median Dice scores were 0.62 (Turbovoxels), 0.53 (Cellpose) and 0.05 (Mesmer). The 2D (slice by slice) median Dice score for Mesmer was much higher at 0.71, indicating that generating 3D results using stitching was a major source of error. For Mesmer the average volume of the segmented myocytes was only about half the volume of that of the ground truth myocytes, while Turbovoxels and Cellpose gave superior results (see Supplementary material for details). The stitching errors also affects the nuclear count per myocyte. As expected, the orientation analysis is consistent across the three methods (Fig. 4). Overall, our experiments confirm both that nuclei within cardiomyocytes are elongated and that their orientations match those of the underlying myocytes quite closely, as observed qualitatively in the literature [2, 10].

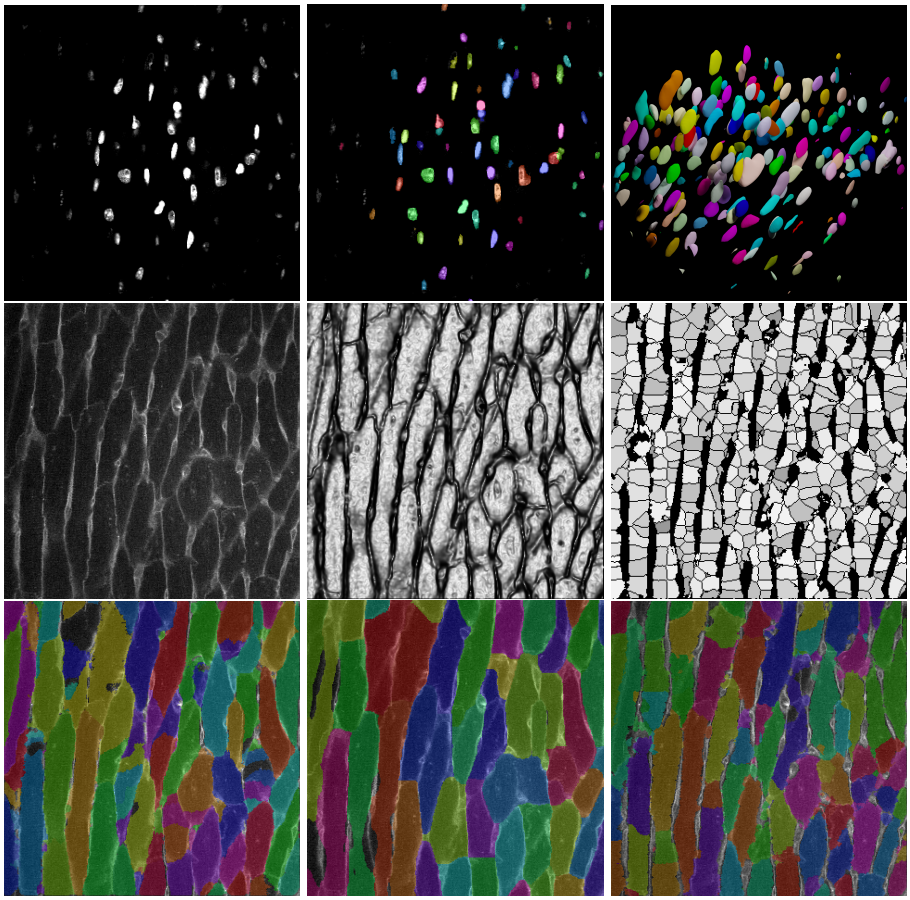

Fig. 3. Top: A DAPI channel image (left) with a sample slice of segmented nuclei using Cellpose (middle) and rendered in 3D (right). Middle: The associated WGA channel image (left), its edge-strength based speed function (middle) (see Section 2.2) and the initial Turbovoxels (right). Bottom: Myocyte boundaries segmented from the edge-strength based speed function using Cellpose (left), Mesmer (middle) and by merging Turbovoxels into Turboblobs (right).

4 Discussion

In microscopy the acquisition of labeled data to train neural network models remains a challenge, although the community is moving towards crowd-sourcing to achieve this [17, 9]. For cleared excised heart wall tissue samples, virtually no such labeled data presently exists. Hence, we deemed that a classic theme in the computer vision and image analysis literature, that of following dense oversegmentation with merging, was appropriate. Our examinations using 3D confocal microscopy show that the estimated orientation differences between

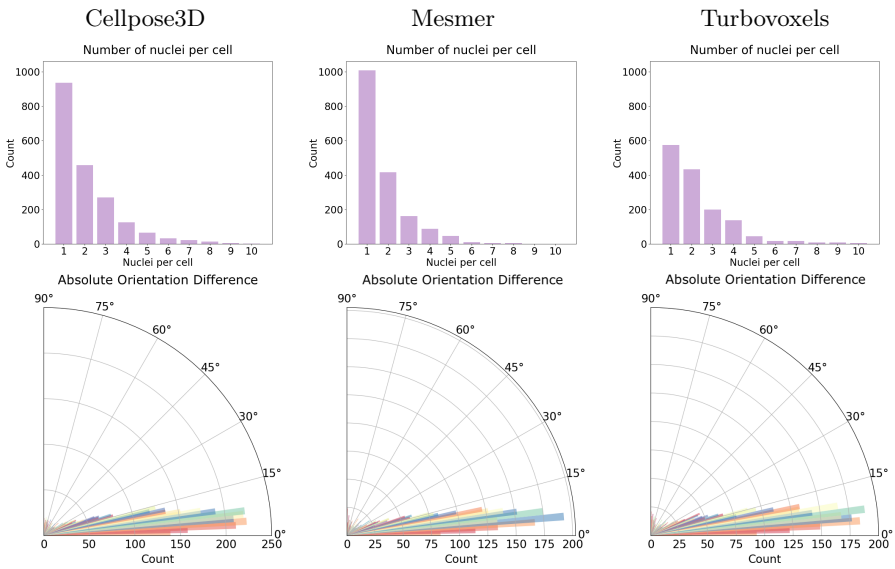

Fig. 4. The number of nuclei per segmented myocyte (top) and histograms of the magnitude of the orientation difference in degrees between myocytes and nuclei (bottom). From left to right: Cellpose3D, Mesmer, Turbovoxels.

cardiomyocytes and their nuclei were consistent with those obtained using deep learning based general cell segmentation models and that cardiomyocytes align with their nuclei. There is some discrepancy between estimates of the number of nuclei across the methods, which could be due to the failure of 2D deep learning based models such as Mesmer to work in 3D. Qualitative inspection showed that Cellpose and Mesmer also tend to include the cell membrane as part of the segmentation result. Turbovoxels, followed by merging, is implemented as a native 3D method and it could be that it leads to larger segmented myocytes on average.

Given enough ground truth data, neural network based approaches have the advantage of having learned from many past examples and of capturing multi-scale relationships in an implicit way, due to their pyramidal architectures. Purely bottom up geometric flow based approaches such as Turbovoxels use much weaker input data. Our demonstration that they are still successful suggests that they might be able to provide pseudo-ground truth cardiomyocyte labels for training neural network models for novel datasets for heart wall ultrastructure analysis.

References

1. Arnoczky, S.P., Lavagnino, M., Whallon, J.H., Hoonjan, A.: In situ cell nucleus deformation in tendons under tensile load; a morphological analysis using confocal laser microscopy. Journal of orthopaedic research **20**(1), 29–35 (2002)

2. Bensley, J.G., De Matteo, R., Harding, R., Black, M.J.: Three-dimensional direct measurement of cardiomyocyte volume, nuclearity, and ploidy in thick histological sections. Scientific reports **6**(1), 1–10 (2016)
3. Bera, M., Kumar, R., Sinha, B., Sengupta, K.: Nuclear deformation and anchorage defect induced by dcm mutants in lamin a. bioRxiv p. 611665 (2019)
4. Bray, M.A.P., Adams, W.J., Geisse, N.A., Feinberg, A.W., Sheehy, S.P., Parker, K.K.: Nuclear morphology and deformation in engineered cardiac myocytes and tissues. Biomaterials **31**(19), 5143–5150 (2010)
5. Brayson, D., Ehler, E., dos Remedios, C.G., Shanahan, C.M.: Analysis of cardiomyocyte nuclei in human cardiomyopathy reveals orientation dependent defects in shape. medRxiv (2020)
6. Chung, K., Wallace, J., Kim, S.Y., Kalyanasundaram, S., Andalman, A.S., Davidson, T.J., Mirzabekov, J.J., Zalocusky, K.A., Mattis, J., Denisin, A.K., et al.: Structural and molecular interrogation of intact biological systems. Nature **497**(7449), 332 (2013)
7. Derks, W., Bergmann, O.: Polyploidy in cardiomyocytes: roadblock to heart regeneration? Circulation research **126**(4), 552–565 (2020)
8. Entcheva, E., Bien, H.: Tension development and nuclear eccentricity in topographically controlled cardiac syncytium. Biomedical Microdevices **5**(2), 163–168 (2003)
9. Greenwald, N.F., et al.: Whole-cell segmentation of tissue images with human-level performance using large-scale data annotation and deep learning. Nature Biotechnology **40**(4), 555–565 (2022)
10. Hussain, A., Ghosh, S., Kalkhoran, S.B., Hausenloy, D.J., Hanssen, E., Rajagopal, V.: An automated workflow for segmenting single adult cardiac cells from large-volume serial block-face scanning electron microscopy data. Journal of structural biology **202**(3), 275–285 (2018)
11. Levinshtein, A., Stere, A., Kutulakos, K.N., Fleet, D.J., Dickinson, S.J., Siddiqi, K.: Turbopixels: Fast superpixels using geometric flows. IEEE transactions on pattern analysis and machine intelligence **31**(12), 2290–2297 (2009)
12. Malandain, G., Fernández-Vidal, S.: Euclidean skeletons. Image and vision computing **16**(5), 317–327 (1998)
13. Maniotis, A.J., Chen, C.S., Ingber, D.E.: Demonstration of mechanical connections between integrins, cytoskeletal filaments, and nucleoplasm that stabilize nuclear structure. Proceedings of the National Academy of Sciences **94**(3), 849–854 (1997)
14. Miko, M., Kyselovic, J., Danisovic, L., Barczi, T., Polak, S., Varga, I.: Two nuclei inside a single cardiac muscle cell. more questions than answers about the binucleation of cardiomyocytes. Biologia **72**(8), 825–830 (2017)
15. Seelbinder, B., Ghosh, S., Schneider, S.E., Scott, A.K., Berman, A.G., Goergen, C.J., Margulies, K.B., Bedi, K.C., Casas, E., Swearingen, A.R., et al.: Nuclear deformation guides chromatin reorganization in cardiac development and disease. Nature biomedical engineering **5**(12), 1500–1516 (2021)
16. Sethian, J.A.: Level set methods and fast marching methods: evolving interfaces in computational geometry, fluid mechanics, computer vision, and materials science, vol. 3. Cambridge university press (1999)
17. Stringer, C., Wang, T., Michaelos, M., Pachitariu, M.: Cellpose: a generalist algorithm for cellular segmentation. Nature Methods **18**(1), 100–106 (2021)
18. Versaevel, M., Grevesse, T., Gabriele, S.: Spatial coordination between cell and nuclear shape within micropatterned endothelial cells. Nature communications **3**(1), 1–11 (2012)

Ultrastructure analysis of cardiomyocytes and their nuclei: supplementary materials

Tabish A. Syed[1 [0000−0002−6987−4975]], Yanan Wang[1 [0000−0002−4427−8667]], Drisya Dileep[2,3 [0000−0002−7871−5343]], Minhajuddin Sirajuddin[2 [0000−0001−5742−2130]], and Kaleem Siddiqi[1 [0000−0002−7347−9716]]

[1] School of Computer Science, McGill University, Montréal, Canada
[2] Institute for Stem Cell Science and Regenerative Medicine, Bengaluru, India
[3] The University of Trans-Disciplinary Health Sciences and Technology (TDU), Bengaluru, India

We provide a number of additional experimental results as supplementary material. These include: The number of nuclei per segmented cell and the absolute differences in orientations for a volume for which we have manually generated ground truth labels (Fig. 1), an illustration of a segmentation failure case (Fig. 2), Dice scores computed in 2D slices alone versus those in 3D (Fig. 3), the mean volume of the auto-segmented myocytes (Fig. 4) and a visualization of stages in the merging process for Turbovoxels (Fig. 5).

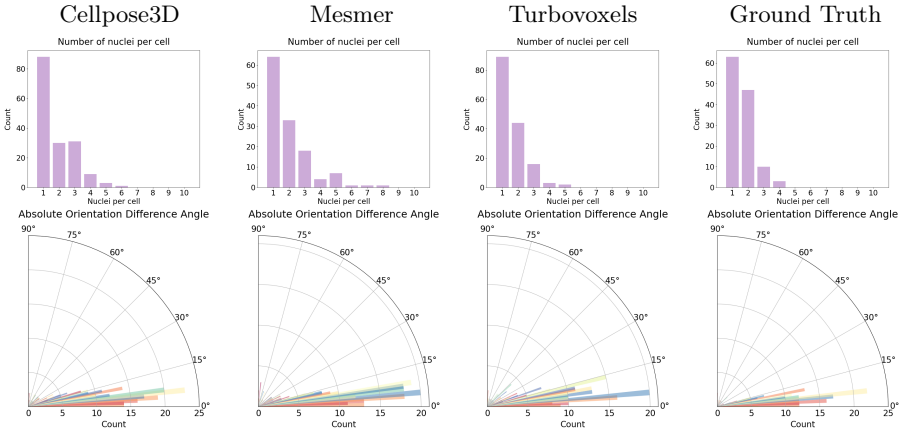

Fig. 1. The number of nuclei per segmented myocyte (top) and histograms of the magnitude of the orientation difference in degrees between myocytes and nuclei (bottom) for a single volume with ground truth labels. From left to right: Cellpose3D, Mesmer, Turbovoxels, Ground truth. In all cases the nuclei are segmented using Cellpose's nucleus option. The total number of nuclei per myocyte varies with the segmentation results.

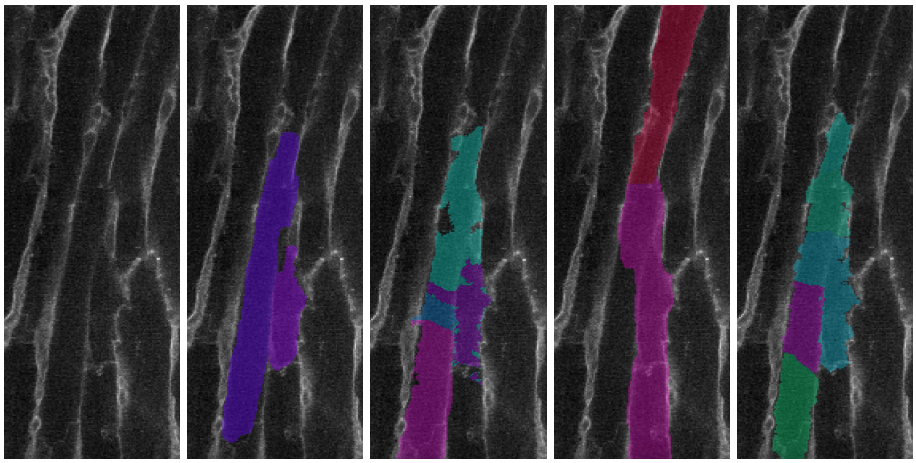

Fig. 2. We illustrate a segmentation failure case by zooming in on a 2D region of a sample volume slice on the left. Overlays of the ground truth segmentation and the results of Cellpose, Mesmer and Turbovoxels are then shown from left to right.

Method	Dice (mean)	Dice (median)	Dice 2D (mean)	Dice 2D (median)
Turbovoxels	0.5710	0.6183	0.4965	0.5868
2D-Cellpose	0.1472	0.0136	0.6228	0.7434
Cellpose	0.4869	0.5359	0.4475	0.5027
Mesmer	0.2113	0.0525	0.6215	0.7144

Fig. 3. The mean and median Dice scores between segmentations and groundtruth labels, for several methods, including 2D-Cellpose, which uses the Cellpose model per slice. The "2D" Dice scores are averages over each 2D slice of the volumes, instead of over entire 3D segmented regions.

Method	Mean Volume(μm^3)	Fraction of GT
Ground truth(GT)	12254	1
Mesmer	6282	0.5126
Cellpose	10829	0.8837
Turbovoxel	12272	1.0014

Fig. 4. The average volume (in μm^3) of ground truth (GT) and auto-segmented myocytes. The Turbovoxel segmented myocytes have about the same average volume as the GT, while Mesmer segmented myocytes are only half the size, a sign of oversegmentation.

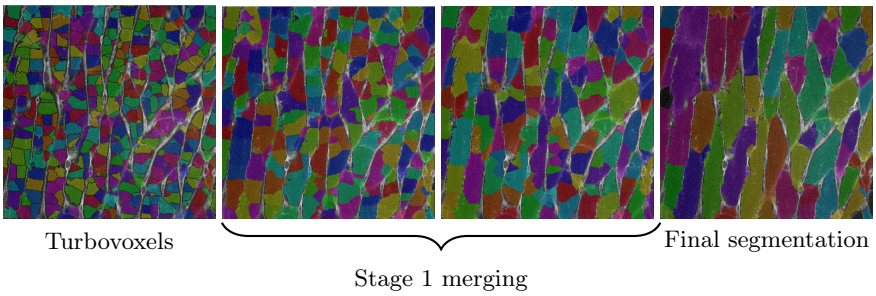

Fig. 5. A visualization of a sample 2D slice from a 3D volume, to illustrate stages of the merging process in the Turbovoxels algorithm. For each stage we overlay the segmented regions on the original raw data (shown in greyscale): initial Turbovoxels (left), stage 1 (middle), and the final segmentation (right).